

Light and thermal responses of liquid-crystal-network films: A finite element study

Hayoung Chung, Joonmyung Choi, Jung-Hoon Yun, and Maenghyo Cho*

Division of Multiscale Mechanical Design, School of Mechanical and Aerospace Engineering, Seoul National University, San 56-1, Shillim-Dong, Kwanak-Ku, Seoul 151-744, South Korea

(Received 9 January 2015; published 10 April 2015)

As a polymeric system incorporating rigid molecules within its structure, the liquid-crystal network (LCN) has been envisaged as a novel heterogeneous material. Under the influence of external stimuli, the orientational order of the liquid-crystalline phase becomes dilute and overall anisotropy is hence decreased; the actinic light absorbed by photochromic molecules, for example, induces the geometric isomerization and subsequently yields internal stress within the local network. In this study we investigate light- and temperature-induced spontaneous deformations of the LCN structure via a three-dimensional finite element model that incorporates geometric nonlinearity with a photomechanical constitutive model. We first examine the bending behavior and its nonlinearity and then parametrically study the various behaviors that stem from different origins ranging from the microscale to the macroscale: (i) the geometry of the LCN film, (ii) the macroscopic global order, (iii) the distorted mesogenic orientation due to the Fredericks distortion, and (iv) defect-induced instability. These interrelated behaviors demonstrate both the simulation capability and the necessity of the presenting framework. By employing a nonlinear consideration along with a microscopic shape parameter r the present approach facilitates further understanding of photomechanical physics such as the deconvolution of various stimuli and the deformed shape obtained due to snap-through instability. Furthermore, this study may offer insight into the design of light-sensitive actuation systems by deepening our knowledge and providing an efficient measure.

DOI: [10.1103/PhysRevE.91.042503](https://doi.org/10.1103/PhysRevE.91.042503)

PACS number(s): 64.70.M-, 61.30.Gd, 61.30.Vx, 02.70.Dh

I. INTRODUCTION

A liquid-crystal network (LCN) broadly refers the polymeric system composed of long, flexible chains and short, rigid, rodlike liquid-crystal mesogenic units. As liquid-crystal molecules impose crystalline order to the molecular chains via cross-linking, this material has been envisaged to yield interesting phenomena, for example, increased (decreased) polymer anisotropy in order to accommodate the increased (decreased) orientational order of the mesogens [1]. For nematic polymers whose liquid-crystalline order possesses only a rotational symmetry, experimental studies have revealed that the material shrinks or expands up to a few hundred percent upon heating or cooling, which renders the material an attractive candidate for artificial muscles [2,3]. Much of our knowledge regarding spontaneous deformation is derived from the Verwey-Warner-Terentjev (VWT) free-energy model, combined with classical polymer physics and phase transition theory. The rotational symmetry of the mesogen units is violated due to molecular thermal vibrations and the initially anisotropic polymeric conformation (i.e., anisotropy radii of the gyration tensor) becomes isotropic. Hence, the polymer chains shrink in the principal direction of the gyration tensor. The overall procedure is captured by the nematic-isotropic transition temperature T_{NI} , which differentiates two distinct phases, along with the shape parameter r , which represents the polymeric conformations [4–6].

Recently, a few studies [7–10] have reported on the reversible bending of LCN-based materials in response to optical stimuli when the photochromic azobenzene molecules are cross-linked to either elastomeric or glassy bases. Provided photons with adequate frequency are incident to the surface

of the system, initially trans- (chair-shape) state molecules change their form into cis- (boat-shape) state molecules through isomerization. Meanwhile, the absorption of photon energy during photoisomerization attenuates the light intensity as the photons travel in the out-of-plane direction. Differential photoinduced strain is thereby produced and generates bending as a consequence. As an increased number of kinked molecules reduces the T_{NI} [11,12], the polymer conformation is strongly responsive to light irradiation. Several applications have been suggested for employing such light-induced motion into actuation systems that are both practical and intriguing [13–15]. In addition, schematic approaches toward behavior control have also been pursued from various perspectives in order to exploit the multiscale and multiphysical nature of the LCN material. For example, such approaches might consider the selection of molecular shape and LCN backbone structure [6,16–18], the microscopic domain design [19–21], or perhaps the modulation of optical stimuli [7,22].

In addition to rich discussions found in the field of anomalous phase behavior, such as that of soft elasticity (i.e., barrier-free director rotations and nonconvexity of VWT energy [23–25]), numerical models to describe the observed bending phenomena [26–28], microcoupling and macrocoupling [29,30], and dynamic nonlinearity ascribed to the light-reflection model [31] have been suggested. To further investigate the mechanism by which photoinduced microscopic change leads to macroscopic nonlinear deformation, we employ a finite-element-based approach with the following constraints: (i) Apropos of the discussion of LCN heating, microscopic observables must be included with regard to optical stimuli; (ii) the method should be able to simulate large deformations, especially those related to bending, twisting, and geometric instability; and (iii) the method must provide the user with modeling capabilities in both microdesign (e.g., backbone order Q_b to optical order Q relation, spatially

*Corresponding author: mhcho@snu.ac.kr

distributed mesogen \mathbf{n}) and macrodesign parameters [e.g., three-dimensional (3D) domain shape and polarity of incident light].

In this study we investigate the light- and temperature-induced motion of the LCN film via finite element formulation, which combines geometric nonlinearity with light-temperature-order coupling behavior. To model the dependence of material deformation on incident light, we used a quasisoft elasticity model proposed by Lin *et al.* [30], which provides a full tensorial description of the material behavior with the aid of a continuum expression of the VWT model [25]. Although restricted to the 2D linear regime, their quasisoft model captures the distinctive properties of LCNs, such as their director rotation and spontaneous deformations. This model is satisfying from the perspective of material properties and light-induced deformation, both of which are described by an initial director \mathbf{n}_0 and a polymer shape r . Assuming that the material undergoes locally linear deformation upon irradiation, the element-independent corotational (EICR) formulation [32] is used to model geometric nonlinearity. Local deformation is hence obtained from global displacement by accounting for the rigid-body motion for which the deformation of the material remains small while large shape distortion is observed (i.e., rotation-dominated bending).

This paper is organized as follows. In Sec. II we present the theoretical basis of photomechanics and the finite element formulation. First, we present a brief description of the derivation of the 3D tensorial constitutive equations from the VWT free-energy model, along with the subsequent reduction of the 3D formula by a 2D plane-stress assumption. Next, the constitutive equation is combined with the nonlinear finite element formulation. Short reviews of the corotational formulation and finite element formulation using photomechanical models are given. In Sec. III we present the light-induced bending curvature in terms of penetration depth and increasing light intensity and discuss this in terms of nonlinearities. Parametric studies of LCN film shape and the uniform rotation of the director are conducted in order to reveal the effect of the extrinsic (postsynthesis) condition of the LCN structure. Finally, we investigate the effect of intrinsic (presynthesis), microscopic design parameters, focusing on the spatially varying mesogenic alignment. By comparing these parametric studies with available experiments, the consideration on geometric nonlinearity is proven to be essential when it is combined with photomechanical aspect; the coupling of the microstructure formation with regard to a macroscopic large deformation not only enhances the modeling capability but grants rich physics to the spontaneous behavior. Most of all, the large shape change due to comprehensive external stimuli and the relaxed configuration of the LCN under mechanical frustration demonstrates the gained insight in terms of both physics and mechanical design.

II. BACKGROUND

In this section we describe the theoretical basis of the proposed model: an implementation of multiphysical light-thermo-order coupling into the finite element formulation combined with geometric nonlinearity. First, we briefly discuss classical LCN modeling via tensorial expression [30], which forms the basis of the constitutive relation. Polymeric confor-

mations and directional anisotropy are parametrized according to the shape parameter r , from which stiffness change and photostress evolutions are determined. Next we embed the photomechanical constitutive equation into a finite element formulation via the variational principle. By combining a 3D shell with 18 degrees of freedom with conditions of geometric nonlinearity, we obtain a generic model for thin LCN structures with large deformation upon irradiation and heating. Concise descriptions of the previous literature regarding photomechanical modeling and geometric nonlinearity with higher-order shell elements are presented as a complement.

A. Photomechanics

1. Tensorial form of the constitutive relation

For nematic LCNs, photomechanical behavior refers to the spontaneous deformation induced by optical or thermal stimuli and originates from a strong connections between various areas of physical study, for example, polymeric backbone conformation and the transition between liquid-crystalline phases (nematic vs isotropic). As demonstrated in the VWT model ($f = \mu/2[\text{tr}(\mathbf{L}^{-1}\boldsymbol{\lambda}\mathbf{L}_0\boldsymbol{\lambda}^T) + \ln(\det\mathbf{L}/\det\mathbf{L}_0)]$), whose derivation is a consequence of statistical descriptions regarding entropic chains and their mesogenic constituents, the shape tensor \mathbf{L} and deformation gradient $\boldsymbol{\lambda}$ exhibit strong coupling. Many of the experimental results about intrinsic phenomena of LCNs, for example, soft elasticity (\mathbf{L} being changed by $\boldsymbol{\lambda}$) and spontaneous deformation ($\boldsymbol{\lambda}$ being changed by \mathbf{L}) [4,23,24], have been widely discussed with regard to the coupling.

Recently, a full tensorial description for the constitutive model was devised by adopting the VWT model and complementing it with a Landau–de Gennes expansion and by further considering the first and second laws of thermodynamics with additional kinematic constraints (see Ref. [25] for a detailed derivation). It is worth mentioning that the introduction of a polymeric conformation tensor \mathbf{g} , which coincides with a scaled shape tensor (i.e., $\mathbf{g} = \mathbf{L}/\det\mathbf{L}$), is crucial during the derivation, as it relates incompressible change between nematic to isotropic configuration and provokes coaxiality while retaining physical features of the polymeric conformation

$$\boldsymbol{\sigma} = -p\mathbf{I} + \mu\mathbf{g}^{-1}(\boldsymbol{\lambda}\mathbf{g}_0\boldsymbol{\lambda}^T) = -p\mathbf{I} + \mu\mathbf{g}^{-1}\mathbf{B}_m. \quad (1)$$

As shown in Eq. (1), the Cauchy stress $\boldsymbol{\sigma}$ is presented as a function of the shear modulus μ , hydrostatic pressure p , effective left Cauchy-Green tensor $\mathbf{B}_m = \boldsymbol{\lambda}\mathbf{g}_0\boldsymbol{\lambda}^T$, and the current metric \mathbf{g} ; coaxiality between the two parameters is found at equilibrium and hence forms a basis of soft elasticity, which explains the stress-free rotation of mesogenic average orientation upon perpendicular stretching.

A tensorial description is directly incorporated into the classical finite element formulation, once it is linearized via the assumption of infinitesimal strain. Although it discourages large stretching and the accompanying stiffness change, the assumption is valid as long as spontaneous deformation with relatively small rotation and strain is considered. The linearized model is hence beneficial to simplifying the photomechanical behavior of LCNs and implementing the finite element; in addition, the linearized approach used in this study [30] prevents complex nonconvexity that requires additional assumptions or solving techniques [23–25,29].

An observable shape parameter r , the square of the ratio between the backbone radius of gyration [6] tensor calculated parallel R_{\parallel} and perpendicular R_{\perp} to \mathbf{n} , is introduced to represent the degree of anisotropy of the metric tensor

$$\mathbf{g} = r^{-1/3}\mathbf{I} + (r^{2/3} - r^{-1/3})\mathbf{nn}, \quad r = (R_{\parallel}/R_{\perp})^2. \quad (2)$$

As a result, the following linearized constitutive relation is thus derived as Eq. (3a); a detailed derivation can be found in Ref. [30]. Strong mechanical-order coupling is presented as reported by both theory and experiment [33]; that is, stress becomes a function of not only strain $\boldsymbol{\varepsilon}$ but also rotation $\boldsymbol{\omega}$ and the shape parameter r . Along with the constitutive equations, the infinitesimal effective strain $\boldsymbol{\varepsilon}_g$ and the director rotation $\delta\mathbf{n}$ are also presented. It is worth mentioning that the director rotation is determined not only by strain but also by the rotation of the elements and is perpendicular to the initial director \mathbf{n} . As depicted in Eq. (3b), biaxiality and inner coupling are exempt from the equation since they are not invoked by light-induced deformation that is parallel to the director [25]:

$$\begin{aligned} \boldsymbol{\sigma} = & -p\mathbf{I} + 2\mu\left(\frac{r}{r_0}\right)^{1/3} \left\{ \boldsymbol{\varepsilon} - \left[1 - \frac{r_0 + 1}{2(r_0 - 1)} \frac{r_0 - r}{r} \right] \right. \\ & \times [\mathbf{n}_0(\boldsymbol{\varepsilon} \cdot \mathbf{n}_0) + (\boldsymbol{\varepsilon} \cdot \mathbf{n}_0)\mathbf{n}_0] + \frac{2r_0}{r} \frac{r - 1}{r_0 - 1} (\mathbf{n}_0 \cdot \boldsymbol{\varepsilon} \cdot \mathbf{n}_0)\mathbf{n}_0\mathbf{n}_0 \\ & \left. + \frac{r_0 - r}{2r} [\mathbf{n}_0\mathbf{n}_0 + \mathbf{n}_0(\boldsymbol{\omega} \cdot \mathbf{n}_0) + (\boldsymbol{\omega} \cdot \mathbf{n}_0)\mathbf{n}_0] \right\}, \quad (3a) \end{aligned}$$

$$\mathbf{B}_m \cdot \mathbf{n} = b_m \mathbf{n},$$

$$\begin{aligned} b_m = & r_0^{2/3} + \mathbf{n}_0 \cdot (\mathbf{H}\mathbf{g}_0 + \mathbf{g}_0\mathbf{H}^T) \cdot \mathbf{n}_0 = r_0^{2/3} + 2\mathbf{n}_0 \cdot \boldsymbol{\varepsilon}_g \cdot \mathbf{n}_0, \\ \delta\mathbf{n} = & \frac{2r_0^{1/3}}{r_0 - 1} \{ \boldsymbol{\varepsilon}_g \cdot \mathbf{n}_0 - (\mathbf{n}_0 \cdot \boldsymbol{\varepsilon}_g \cdot \mathbf{n}_0)\mathbf{n}_0 \}. \quad (3b) \end{aligned}$$

Equation (4) explains additional assumptions made to model the thin LCN sheets (reported in the experiments of Refs. [8,9,19]) whose length-to-thickness ratio was smaller than 1:20. The assumptions express (a) plane stress, (b) how the initially homogeneous directors remain homogeneous after the light-induced order change, and (c) incompressibility:

$$\sigma_{3i} = 0, \quad (4a)$$

$$n_3^0 = n_3 = 0, \quad (4b)$$

$$\text{tr}(\boldsymbol{\varepsilon}) = 0. \quad (4c)$$

The 2D constitutive equation is thus expressed by Eq. (5) for plane stress conditions (the greek indices are 1 or 2), which can be readily implemented into a 3D shell model:

$$\begin{aligned} \sigma_{\alpha\beta} = & 2\mu\left(\frac{r}{r_0}\right)^{1/3} \left[-\delta_{\alpha\beta}(\varepsilon_{11} + \varepsilon_{22}) + \varepsilon_{\alpha\beta} \right. \\ & - \left\{ 1 - \frac{r_0 + 1}{2(r_0 - 1)} \frac{r_0 - r}{r} \right\} \{ \varepsilon_{\beta\gamma} n_{\alpha}^0 n_{\gamma}^0 + \varepsilon_{\alpha\gamma} n_{\beta}^0 n_{\gamma}^0 \} \\ & + \left(\frac{2r_0}{r} \frac{r - 1}{r_0 - 1} \right) (\varepsilon_{\eta\psi} n_{\eta}^0 n_{\psi}^0) n_{\alpha}^0 n_{\beta}^0 \\ & \left. + \frac{r_0 - r}{2r} \{ n_{\alpha}^0 n_{\beta}^0 + \omega_{\beta\gamma} n_{\alpha}^0 n_{\gamma}^0 + \omega_{\alpha\gamma} n_{\beta}^0 n_{\gamma}^0 \} \right] \\ \hat{=} & \sigma_{\alpha\beta}^0(\varepsilon_{\alpha\beta}, \omega_{\alpha\beta}, n_{\alpha}^0; r, r_0) + \sigma_{\alpha\beta}^{\text{ph}}(n_{\alpha}^0; r, r_0). \quad (5) \end{aligned}$$

As shown, the effects of external stimuli must be expressed in relation to the shape parameter; most discernible changes from previous models [26,31] and the phenomenological continuum model [4] are in the form of photoinduced stress $\sigma_{\alpha\beta}^{\text{ph}}$ as an eigenstress form, where arbitrary numerical values are not required.

2. Light-thermo-order coupling

The most important aspect in the photomechanical response is the correlation between the shape parameter r to incident light I and temperature T . Although this correlation is pivotal, no closed formula has been proposed to elucidate the influence of the existing polymeric backbone to the liquid-crystalline phase and the effect this has upon the increase of geometrically kinked (cis) molecules. In this study an experimentally determined format is used on account of its simplicity; according to the experimental results [6,11], the shape parameter r is

$$r = \begin{cases} [1 + \alpha(T_{NI} - T)^{\zeta}]^3 & \text{for } T \leq T_{NI} \\ 1 & \text{otherwise,} \end{cases}$$

$$T_{NI}(I) = T_{NI}^0 - \beta \cdot n_{\text{cis}}(I), \quad (6)$$

with α (optical-mechanical-order coupling) and ζ (effective critical exponent) representing material-specific parameters. A shift of T_{NI} resulting from light illumination is modeled as a linear dependence on the ratio of photoisomerized cis molecules n_{cis} (with proportionality coefficient β), as shown. It is worth noting that other theories, such as those regarding linear proportionality to light intensity or heat [21,26,34], experimental fitting [31], and molecular theories [17], can possibly be applied as an alternative to this light-temperature-parameter coupling.

In addition, the population dynamics for isomerized molecules is modeled in terms of the light-induced depletion of trans isomers and competing constant-rate recovery. To simplify the steady-state solution n_{cis}^{∞} , an effective light intensity I_{eff} is introduced by multiplying the intensity by the cis state lifetime τ^{-1} and absorption rate Γ :

$$\dot{n}_{\text{cis}} = (\Gamma I)n_{\text{trans}} + \tau^{-1}n_{\text{cis}}, \quad (7a)$$

$$n_{\text{cis}}^{\infty} = \frac{\tau\Gamma I}{1 + \Gamma\tau I} \hat{=} \frac{I_{\text{eff}}}{1 + I_{\text{eff}}}, \quad (7b)$$

$$I_{\text{eff}} = W_L[I_{\text{eff}}^0 \exp(I_e^0 - z/d)]. \quad (7c)$$

Equation (7a) describes the profile of light intensity as a function of the maximal intensity of incident light I_{eff}^0 on the surface of the film, the out-of-plane position from midplane z , and the penetration depth d . According to the photobleaching effect [35], the light intensity decays nonexponentially as the light travels through the polymeric domain and its decay profile is affected by the initial light intensity I_{eff}^0 . The profile of light within the LCN thickness is therefore described by the Lambert W function W_L , which lacks a closed-form solution. The penetration depth d characterizes the saturation depth of light, possibly determined by the interplay between polymer characteristics and the cross-linking ratio of the chain.

The present light-temperature-order model is a legacy from various fields such as polymer physics (the freely jointed

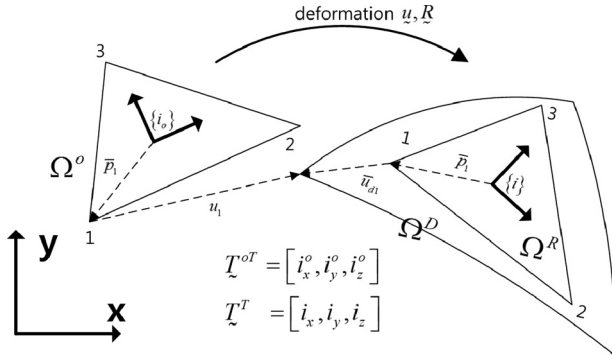


FIG. 1. Kinematics of EICR.

model), phase transition theory, and light decay. The basic formula therefore offers much room for improvement because there are superior methods available for tailoring [36,37] and measuring [12,38] r directly.

B. Geometric nonlinear shell formulation for LCNs

To analyze the deformation of 2D LCN sheets into 3D deformed shapes through bending and twisting [8,9,28], geometric nonlinearity that arises from a significant change of slender LCN geometry is considered in the present work.

Herein, the nonlinear formulation model is based on the corotational formulation approach. The most salient feature of the corotational formulation is the procedure for separating the pure deformation and the rigid-body motion from the displacement of elements. In EICR [32], the separation is based purely on kinematics and thus distinguishable from basic polar decomposition of the deformation gradient; as an external filter, EICR considerations are applied externally to the local elements and thus the strain-displacement relation is completely detached from nonlinear considerations (i.e., element independence). Therefore, we efficiently implement the higher-order element, which thus enhances not only the accuracy of the solution but also reduces the need of reduced integration. Therefore, EICR is the essential tool for the geometric nonlinear solution under consideration. The matrix notation used herein follows that of Ref. [32].

To enable kinematic tracking of rigid-body motions over the element, corotational formulation requires three configurations, as shown in Fig. 1. These are the nondeformed Ω^0 , deformed Ω^D , and corotational Ω^R configurations. The latter is a theoretical concept introduced to mediate between two natural coordinates, based on the premise that the rigid-body part of the total displacement is executed first, before the element is deformed.

The local frame e^i and the local-to-global translation matrix \mathbf{T} are calculated elementwise during each time step. Located at the centroid of each element, the local axis of \mathbf{e}_1 is oriented parallel to side 1-2, whereas \mathbf{e}_3 remains perpendicular to the element. In addition, Ω^R and Ω^D are stated upon the same local frame, as shown in Fig. 1, because the local frame translates and rotates as its base element does. Pure deformation is obtained by comparing the deformed shape with the corotational one, expressed by the pure deformation $\bar{\mathbf{u}}_d$ and the rotation $\bar{\boldsymbol{\theta}}_d$, where an overbar and a subscript

d indicate that the properties refer to the local frame and pure deformation, respectively. A tensorial description for separating the rigid-body motion from the global shape change is given by

$$\delta \bar{\mathbf{d}}_d = \begin{Bmatrix} \delta \bar{\mathbf{u}}_d \\ \delta \bar{\boldsymbol{\theta}}_d \end{Bmatrix} = \bar{\mathbf{H}} \bar{\mathbf{P}} \mathbf{T} \begin{Bmatrix} \delta \mathbf{u} \\ \delta \boldsymbol{\phi} \end{Bmatrix} \equiv \boldsymbol{\Lambda} \begin{Bmatrix} \delta \mathbf{u} \\ \delta \boldsymbol{\phi} \end{Bmatrix}, \quad (8)$$

where $\boldsymbol{\phi}$ is a pseudovector of the nodewise rotator \mathbf{R} and \mathbf{H} , \mathbf{P} , and \mathbf{T} are auxiliary matrices of EICR formulation. Equation (8) demonstrates the sequence of the kinematics-based procedures that define EICR. After the nodal displacement is transformed to the global frame via \mathbf{T} , the deforming part is extracted through the projection matrix \mathbf{P} , which extracts the pure deformation part. The matrix \mathbf{H} eliminates the gap between the two pseudovectors $\boldsymbol{\theta}$ and $\boldsymbol{\phi}$.

The consistent tangent stiffness matrix \mathbf{K} and the local residual force \mathbf{R} are calculated as shown in Eq. (9). A conventional Newton-Raphson algorithm is used to solve the finite element equations. An adaptive step-size control scheme [39] is used and step size is either increased or decreased depending on the stiffness matrix conditions

$$\begin{aligned} \Delta \mathbf{f} &= \mathbf{f}^i - \mathbf{f}^e = \mathbf{T}^T \bar{\mathbf{P}}^T \bar{\mathbf{H}}^T \bar{\mathbf{K}}^e \bar{\mathbf{f}}^e - \mathbf{T}^T \bar{\mathbf{H}}^T \bar{\mathbf{f}}^{\text{ph}} \\ &= \mathbf{T}^T \bar{\mathbf{P}}^T \bar{\mathbf{H}}^T (\bar{\mathbf{K}}^e \bar{\mathbf{d}}_d) - \mathbf{T}^T \bar{\mathbf{H}}^T \bar{\mathbf{f}}^{\text{ph}}. \end{aligned} \quad (9)$$

In Eq. (9) $\bar{\mathbf{f}}^e = \bar{\mathbf{K}}^e \bar{\mathbf{d}}_d$ is the local force and $\bar{\mathbf{f}}^{\text{ph}}$ is the photostress force. The projection matrix is removed for the light-induced force term because the rigid-body part of the external load should not be subtracted out, as in the case of the force

$$\begin{aligned} \mathbf{K} &= \mathbf{K}^i - \mathbf{K}^e = (\mathbf{K}_{GR}^i + \mathbf{K}_{GP}^i + \mathbf{K}_{GM}^i + \mathbf{K}_M^i) \\ &\quad - (\mathbf{K}_{GR}^e + \mathbf{K}_{GM}^e), \end{aligned} \quad (10)$$

with

$$\begin{aligned} \mathbf{K}_M &= \mathbf{T}^T \bar{\mathbf{P}}^T \bar{\mathbf{H}}^T \bar{\mathbf{K}}^e \bar{\mathbf{H}} \bar{\mathbf{P}} \mathbf{T}, \quad \mathbf{K}_{GR} = -\mathbf{T}^T \bar{\mathbf{F}}_{nm} \bar{\mathbf{G}} \mathbf{T}, \\ \mathbf{K}_{GM} &= \mathbf{T}^T \bar{\mathbf{P}}^T \bar{\mathbf{L}} \bar{\mathbf{P}} \mathbf{T}, \quad \mathbf{K}_{GP} = -\mathbf{T}^T \bar{\mathbf{G}}^T \bar{\mathbf{F}}_n \bar{\mathbf{P}} \mathbf{T}, \\ \mathbf{K}_{GM}^e &= \mathbf{T}^T \bar{\mathbf{L}}^e \bar{\mathbf{P}} \mathbf{T}, \quad \mathbf{K}_{GR}^e = -\mathbf{T}^T \bar{\mathbf{F}}_{nm}^e \bar{\mathbf{G}} \mathbf{T}. \end{aligned} \quad (11)$$

As shown in Eq. (11), the stiffness matrices are categorized according to the source of nonlinearity; the subscripts M , GR , GM , and GP stand for the variations of matrices \mathbf{f} , \mathbf{T} , \mathbf{H} , and \mathbf{P} , respectively. Terms with the superscript e denote illumination-induced geometric stiffness and are calculated consistently with $\bar{\mathbf{f}}^{\text{ph}}$.

The finite element formulation of the linear element is constructed by using the variational principal; its derivation is given by

$$\begin{aligned} \delta W &= \int_V \delta u_i \sigma_{ij,j} dV = \int_V \nabla (\delta u_i \sigma_{ij}) - \delta u_{i,j} \sigma_{ij} dV \\ &= \int_S \delta u_i t_i dS - \int_V \delta u_{i,j} \sigma_{ij} dV. \end{aligned} \quad (12)$$

The first term on the right-hand side accounts for boundary conditions; thus our focus lies with the second term. As shown in Eq. (5), stress is divided into symmetric (strain-related σ_{ij}^e)

and skew-symmetric (rotation-related σ_{ij}^ω) parts

$$\begin{aligned} & \int_V \delta u_{i,j} \sigma_{ij} dV \int_V \delta u_{i,j} (\sigma_{ij}^\varepsilon + \sigma_{ij}^\omega) dV \\ & = \int_V \delta \varepsilon_{ij} \sigma_{ij}^\varepsilon dV + \int_V \delta \omega_{ij} \sigma_{ij}^\omega, \end{aligned} \quad (13)$$

with $\omega_{ij} = (u_{i,j} - u_{j,i})/2$. Due to the skew symmetry of element rotation tensor and corresponding rotation term, $\sigma_{ij}^\omega = -\sigma_{ji}^\omega$ strain-rotation coupling is removed from the equations. Therefore, the formulation for each shell element is

$$\begin{aligned} \delta W & = \int_\Omega \delta (\boldsymbol{\varepsilon}^0 - z\mathbf{k})^T (\boldsymbol{\sigma}^0 - \boldsymbol{\sigma}^{\text{ph}}) dV \\ & \equiv \delta \bar{\mathbf{d}}_d \cdot \bar{\mathbf{K}}^e \cdot \bar{\mathbf{d}}_d - \delta \bar{\mathbf{d}} \cdot \bar{\boldsymbol{\Sigma}}^{\text{ph}}, \end{aligned} \quad (14)$$

with

$$\bar{\boldsymbol{\Sigma}}^{\text{ph}} = \{\hat{\mathbf{N}}^{\text{ph}}, \hat{\mathbf{M}}^{\text{ph}}\}^T, \quad (15a)$$

$$\bar{\mathbf{K}}^e = [\bar{\mathbf{K}}^m + \bar{\mathbf{K}}^b + 2\bar{\mathbf{K}}^{mb}] - [\bar{\mathbf{K}}^r], \quad (15b)$$

$$\bar{\mathbf{K}}^m = \int \mathbf{B}^{\varepsilon T} \hat{\mathbf{A}} \mathbf{B}^\varepsilon dA, \quad \bar{\mathbf{K}}^b = \int \mathbf{B}^{\kappa T} \hat{\mathbf{D}} \mathbf{B}^\kappa dA,$$

$$\bar{\mathbf{K}}^{mb} = \int \mathbf{B}^{\varepsilon T} \hat{\mathbf{B}} \mathbf{B}^\kappa dA, \quad \bar{\mathbf{K}}^r = \int \mathbf{B}^\phi \hat{\mathbf{G}} \mathbf{B}^\phi dA. \quad (15c)$$

The series of \mathbf{B} matrices in Eq. (15) are strain-displacement matrices unique to the linear element formulation. The superscripts ε , κ , and ϕ are related to strain, curvature, and rotation, respectively. The optimal triangular (OPT) element suggested by Felippa [40] is used to compute the membrane part of the shell behavior, which is denoted by the superscript m . It is based on the assumed natural deviatoric strain formulation, especially optimized for in-plane bending and free from the aspect-ratio locking problem. The OPT elements are used to calculate the \mathbf{B} matrices of the membrane strain and rotation (θ_z, u_x, u_y). On the other hand, discrete Kirchhoff triangular (DKT) elements by Batoz *et al.* [41] are utilized to describe the bending behavior of the shell, which is the strain-curvature relation (θ_x, θ_y, u_z). The bending part of the motion is denoted by the superscript b and it describes the curvature-related part of nodal rotation and displacement. From the Kirchhoff-Love plate theory, it follows that the DKT elements are free from

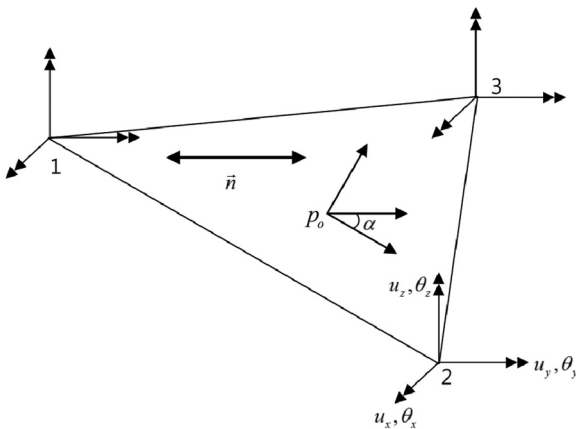


FIG. 2. Three-node shell formulation with 18 DOF and nematic orientation.

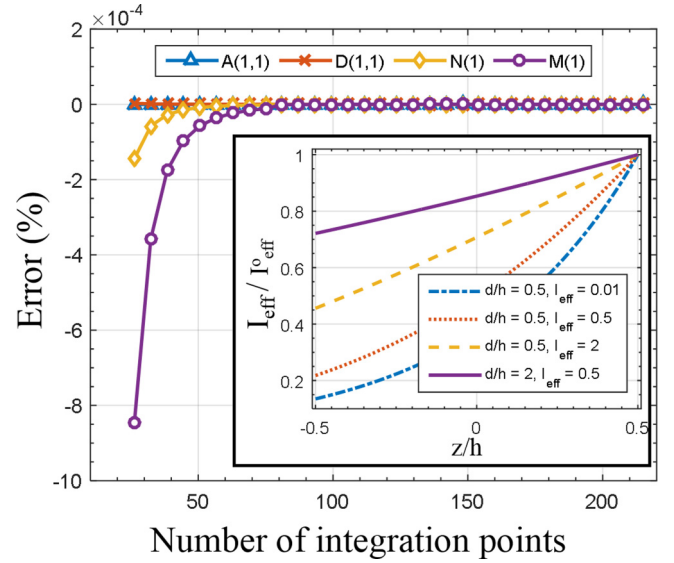


FIG. 3. (Color online) Effect of the number of integration points within a thickness on the numerical integration for midplane properties. The inset shows properties of light decay for various values of penetration depth and intensity.

the shear-locking issue. The construction of 3D triangular elements with 18 degrees of freedom (DOF) is assumed to be a process of unification of two different sets of DOF, as illustrated in Fig. 2. Throughout the computations, we assume that the angle between the local frame axis 1 and nematic orientation α is maintained, in analogy to the direction of the fiber embedded in the composite structure.

Constitutive matrices and eigenstresses are integrated through the LCN sheet thickness to generate a membrane, bending stiffness matrices, and in-plane resultants, all of which are marked by carets. Simpson's numerical integration scheme is used because the properties are affected by the decay of light intensity described by the nonanalytic, high-order Lambert W function. As illustrated in inset of Fig. 3, the profile of light varies from linear to exponential as light intensity and decay depth change. Figure 3 shows the effect of changing the number of integration points on the integrated values, demonstrating that 150 points along the thickness dimension are sufficient for generating stabilized midplane properties in all cases.

III. RESULTS AND DISCUSSION

We now exemplify the simulation capability of our numerical framework by examining the influences from the different physical regime on the light- and heat-induced deformations. The changing parameters range from micro to macro, where the term macroscopic refers to extrinsic material alternatives determined after the synthesis of the polymerized sheet. Similarly, microscopic parameters involve the intrinsic change during the synthesis step and determine the microstates of local mesogenic configuration.

Light-induced bending is first presented in terms of curvatures in the longitudinal direction. Nonlinearities stem from either the photobleaching effect or large geometric

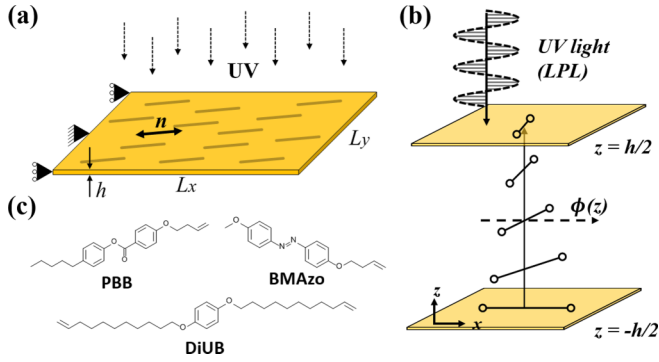


FIG. 4. (Color online) LCN model configurations. (a) Model geometry with length, thickness, and mesogenic director \mathbf{n} . (b) Depthwise angle ϕ between LPL and the director. (c) Structural formula of molecules used herein (components of Azo18 [11]).

deformations; such nonlinearities are found and discussed via comparison to linear solutions. We elucidate the light conditions and temperature stimuli that lead to two solutions.

Parametric studies were also conducted to investigate the photomechanical spontaneous shape change with diverse simulation conditions as the 3D shell finite element formulation adopted in this work facilitates the simulation for a generic LCN model with various shapes and mesogenic quantities. Accordingly, the variation of shape parameter r to both the in-plane and out-of-plane directions enables more detailed modeling regarding the light–heat–order interactions. The influences from macroscopic design parameters are considered first. An ellipsoidal LCN sheet that swims afloat on water [13], along with the directed bending of a cantilevered plate with incident light [7,8], is simulated and discussed in terms of domain shape and mesogenic orientation. Next, we move our focus to the microscopic modulation of the materials. In this context, we find that LCN structures with a spatially distributed director yield highly nonlinear phenomena compared to analytic solutions. We surmise that this discrepancy is induced by either disclination defects [42] or the Fredericks transition [43].

A. Light-induced bending

Figure 4 shows an LCN sheet model, where L_x and L_y denote the length in the x and y directions, respectively; h represents the thickness of the model, and $\phi(z)$ represents the angle between the director \mathbf{n} and the polarization angle of linearly polarized light (LPL), which varies with thickness. Material parameters are set to their experimentally fitted values ($T_{NI}^0 = 340$ K, $\alpha = 0.22$, $\zeta = 0.195$, and $\beta = 11.8$), which correspond to polymeric compositions comprised of pendent- and cross-linked-type molecules (BMAzo, PBB, DiUB; full names of these materials can be found in Ref. [11]). A shear modulus μ is set to 10^4 Pa, following experimental reports [6,11] on elastomeric LCNs.

Due to the spatially graded strain generated in the out-of-plane direction, the LCN strip bends when it is exposed to UV illumination. If the nematic orientation is aligned parallel to the direction of length ($\mathbf{n} \parallel \mathbf{x}$), which generates surface-dominant longitudinal contraction, the LCN strip bends towards the

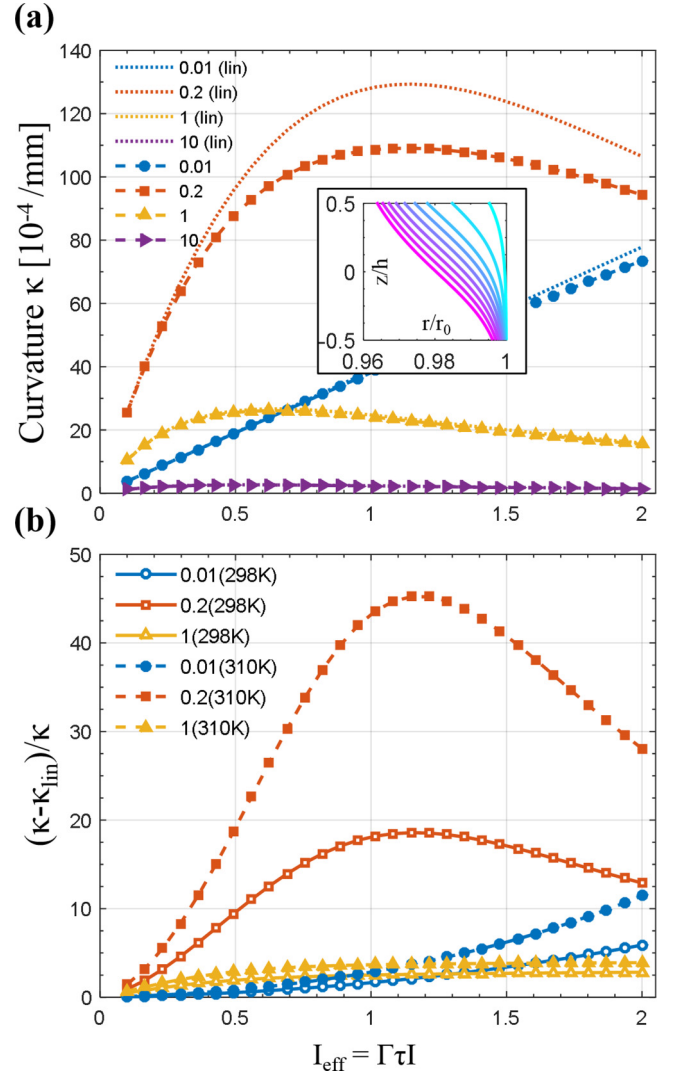


FIG. 5. (Color online) Curvature of the cantilevered LCN ($\mathbf{n} \parallel \mathbf{x}$, $h = 0.5$ mm, $L_x = 10$ mm, and $L_y = 1$ mm) for various penetration depths d . The inset shows the changing profile of the normalized shape parameter r/r_0 (y axis) with weaker [light gray (blue)] and stronger [dark gray (red)] light.

light source. We investigated the effects of light intensity and penetration depth on the bending behavior (Fig. 5). The bending behavior is characterized by the bending curvature κ evaluated through third-order polynomial fitting [Eq. (17)] of the x - z profile of the deformed shape in order to alleviate the complexity of comparing surface curvatures

$$\begin{aligned}
 u_z &= a_i x^i, \quad 0 \leq i \leq 3; \quad i \in \mathbf{Z}, \\
 \kappa(x=0) &= u_z''(x=0)/[1 + u_z'(x=0)^2]^{3/2} \\
 &= 2a_2/(1 + a_1^2)^{3/2}. \quad (16)
 \end{aligned}$$

In Fig. 5(a) the penetration depth d is varied while the temperature T is fixed at 298 K, for which liquid crystals are deeply within the nematic phase. As previous works have asserted [25,30,43], we also find that the bending behaviors are highly nonlinear for increased intensities of light, as they are dependent upon the spatial gradient through the thickness

[see the inset of Fig. 5(a)]. The influence of geometric nonlinearity on the solution is also demonstrated by comparing the curvatures computed from linear and nonlinear finite element solutions. Despite the small curvatures, Fig. 5(b) exhibits the salient gaps between linear (dotted line) and nonlinear (solid line with symbols) solutions for increased temperature. In general, nonlinearity trends follow the profile of deflection as this indicates a higher bending moment; the gap between linear and nonlinear models is profound when the penetration-depth-to-thickness ratio d/h is 0.4, where a maximal gap (44%) is found at the apex of the profile. On the other hand, for d at both extremes (0.01 and 10) compared to the thickness, the deformation is in-plane dominant; therefore, geometric nonlinearity and bending deflection are both restricted. Although not discussed herein, the geometric nonlinearity of the LCN cantilever with uniform mesogenic orientation and thickness has no influence as long as the ratio of light penetration over thickness d/h remains constant.

Concerning the temperature, for an elevated temperature (310 K) lower than the transition temperature T_{NI} ($=340$ K), both curvature discrepancy and displacement increase due to the significant uniform decrease of the shape parameter. These results assert the nonlinear sensitivity of intensity not only to external stimuli, but also to the LCN sheet design criteria, because light-order parameters such as penetration depth d and the phase-light connecting parameter α are determined during the synthesis process [4,11]. Therefore, more extensive experimental and theoretical studies on the synthesis are required because they may enhance the capability of the proposed framework. Incidentally, it is also found that the light intensity at the curvature peak and overall shape do not coincide. This is another indication of nonlinearity because it demonstrates that, contrary to the linear case, larger bending does not necessarily yield larger curvature.

B. LCN design parameters

Having discussed the onset of bending and the nonlinear considerations, we now present the effects of the LCN design parameters on the behavior of LCN sheets. These results evidence the enhanced simulation capability of the present work, showing that it is suitable for photomechanical discussions about generic LCN deformation and design of LCN applications such as actuators and self-folding materials. Most of all, it does not require designed eigenstrain as in the micromechanics-based study [27,28,44], which cannot account for the effect of a changing shape parameter that interacts with the decaying profile of light, and quasirotation of the local order of mesogens [30]. In the following, two types of LCN macroscopic design parameters are examined: anticlastic behavior in an ellipsoidal domain and the effect on the directional orientation.

1. Anticlastic behavior

First, a nonzero Gaussian curvature developed by the illumination of a nonsquare LCN is shown in Fig. 6(a). An initially flat, ellipsoidal sheet with R_x and R_y as its principal radii is examined herein. The nematic director is assumed to be aligned in the x direction without loss of generality. We

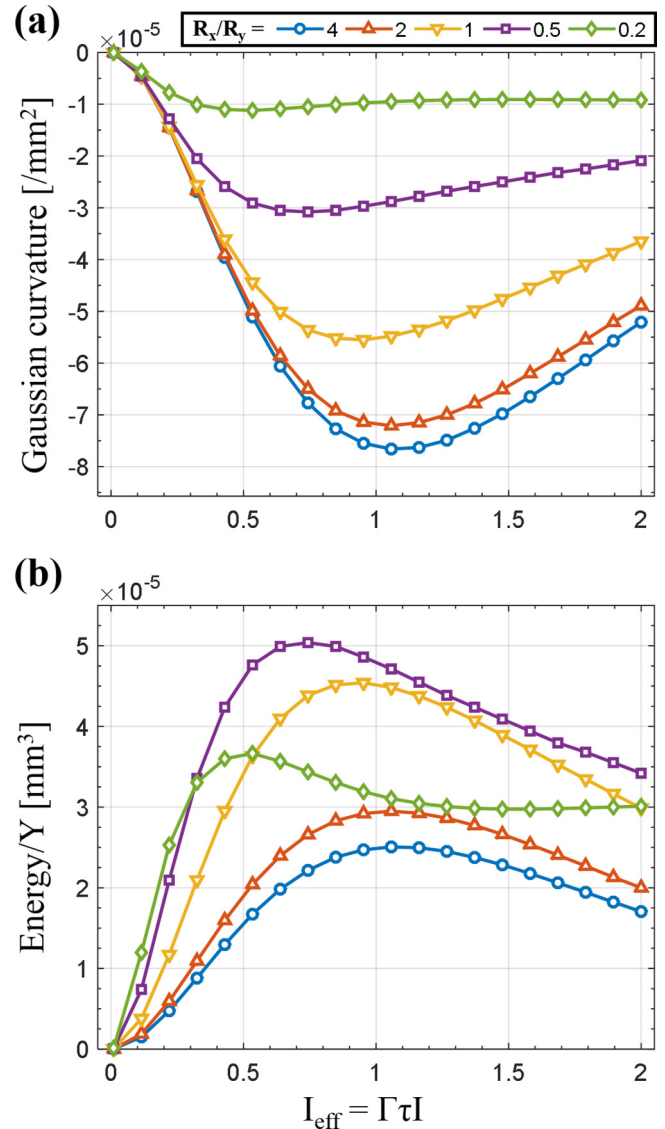


FIG. 6. (Color online) Swimming nonsquare LCN sheet under illumination for different aspect ratios R_x/R_y : (a) Gaussian curvature and (b) estimated strain energy scaled by a modulus.

set the thickness h to 0.5 mm and the penetration depth d to 0.2 mm, which correspond to maximal deflection in the LCN cantilever and are significantly smaller than the fixed value of the LCN sheet's longitudinal radius $R_x = 20$ mm. The curvatures on the surface and local principal axes are computed via the least-squares fitting of the surface composed of local neighboring vertices to a quadratic patch.

The evolution of the saddle shape induced by light irradiation is clearly represented by the developing negative Gaussian curvature, whereas the tipping point of irradiation and maximum curvature vary according to the aspect ratio. We show that shorter length in the direction perpendicular to the nematic direction is preferred for severe anticlasticity generation.

According to the swimming LCN sheet experiment [13], which utilizes the instantaneous emergence of anticlasticity upon irradiation, the induced curvature is closely related to

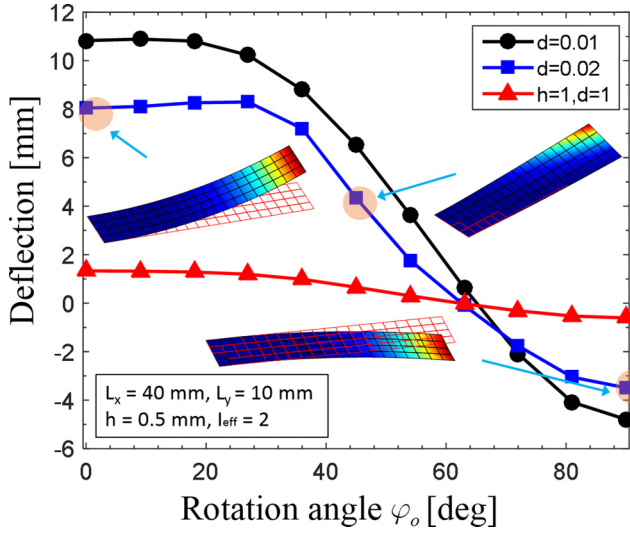


FIG. 7. (Color online) Effect of director rotation on the bending direction and the emergence of twist-bend coupling.

the energy transfer that drives the swimming. Equation (17) illustrates a crude estimation of the energy, where Y is the Young modulus, κ is the Gaussian curvature, h is the thickness, and A is the domain area:

$$\frac{E_{\text{est}}}{Y} = \frac{A h^3}{24 \kappa}. \quad (17)$$

The response of the strain energy shown in Fig. 6(b) also exhibits nonmonotonic behavior. However, a more moderate difference is shown between the energies corresponding to the different aspect ratios, unlike the Gaussian curvature itself. These results assert that the larger aspect ratio is favorable for stronger light intensity in order to achieve the maximal efficiency when the length of the nematic orientation axis is fixed. These findings indicate that designing optimized and efficient actuators requires the investigation of various parameters because stronger light does not necessarily imply more thrusting power and is strongly affected by geometric conditions.

The directed bending driven by in-plane rotation of the globally uniform director is shown in Fig. 7. Such a configuration is fabricated by cutting the specimen out in the nonparallel direction to the monodomain alignment, which alters the principal bending direction. The light is assumed to be nonpolarized without loss of generality and the angle φ_0 is defined as the difference between the x direction and the local orientation \mathbf{n} . It can be clearly seen that maximal tip deflection monotonically decreases as φ_0 increases from 0° to 90° .

Three different light penetration depths are displayed, all of which show a similar trend as torsional deformation replaces bending while their maximal displacement varies. In all cases, the vertical tip deflection becomes zero when the directional difference increases to 60° , after which the sheet starts to bend away from the light. These results agree well with the experimental results obtained for glassy polymers with various director orientations [8].

The point at which zero vertical displacement emerges is another indicator of the nonlinearity need of the 3D shell model

compared with the 2D confined model. When φ_0 is not 0° or 90° , in-plane shear N_{12}^{ph} and torsion M_{12}^{ph} resultants become nonzero by rotation of the principal direction. As a result, the effects of shear and torsion become profound and the tip is moved upward to compensate for the driving momentum. Consequently, this in-plane phenomenon attenuates the occurrence of zero tip deflection and this behavior becomes more profound in the corotational formulation because geometrically driven rigid-body rotation between Ω^0 and Ω^R is added to pure element rotation $\hat{\theta}_z$. In conclusion, the orientation effect results show that n_0 is not only an important design parameter of actuation exhibited by LCN materials, but is also an effective measure for demonstrating the need for the present framework.

2. Effect of directional orientation

We also examine the effect of microstate modulation in the following two examples, focusing on the spatial distribution of the mesogens. A change of principal direction due to the change of mesogen director imprinted on the LCN film is the mechanism underlying the deformation. The twist configuration of mesogens, one of the Fredericks transitions that evolves within the material thickness, is first simulated. In addition to temperature-induced deformation, the shape of which can be determined analytically [28], light intensity and decaying profile-dependent deformation are analyzed. In addition, the effects of polarization of light are also simulated and compared to nonpolarized light. Next, we demonstrate the disclination-defect-driven instability. With the strength being $+1$, the defect generates radially distributed mesogens and hence produces shrinkage in the radial direction, combined with expansion in the azimuthal direction. Therefore, the LCN shell under light irradiation suffers from geometric instability, similar to a bifurcated thermomechanical shell. These two results are important in the sense that such a nontrivial mesogenic director field is nowadays envisaged as a novel measure to modulate the LCN behavior [9,45].

During cross-linking, when liquid-crystal molecules retain their orientational mobility, external conditions (such as mechanical loading) produce depth-dependent mesogenic orientations. In the twist configuration shown in Fig. 8(a), directors remain in plane while the direction gradually changes from top to bottom. This generates eigenstress (or eigenstrain) as a function of depth z , yields maximal anticlastic curvature ($\kappa_{xx} = \kappa_{yy}$) when heated [28], and twists when irradiated [9]. In addition, angles with respect to LPL are also inspected; when the angle of the Poynting vector does not coincide with the axis of the chromophore, the effective intensity of the chromophore extracted from photonic vibrations decreases. The simplest model for such phenomena is given by [17]

$$I_{\text{eff}}(\phi) = I_{\text{eff}}^0 \cos^2(\phi). \quad (18)$$

Figure 8(a) exhibits the modeling of the twist configuration and its effect on the shape parameter r that evolves in the out-of-plane direction. The midplane angle $\phi_0 = \phi(z=0)$ is assumed to be $\pi/4$, while the span of the surface to bottom rotation is fixed at $\pi/2$. When the LPL is incident on the surface, minimal energy is transmitted to the molecules at the top, which smoothly increases as ϕ grows smaller and decreases as the decay of light overwhelms the phenomena.

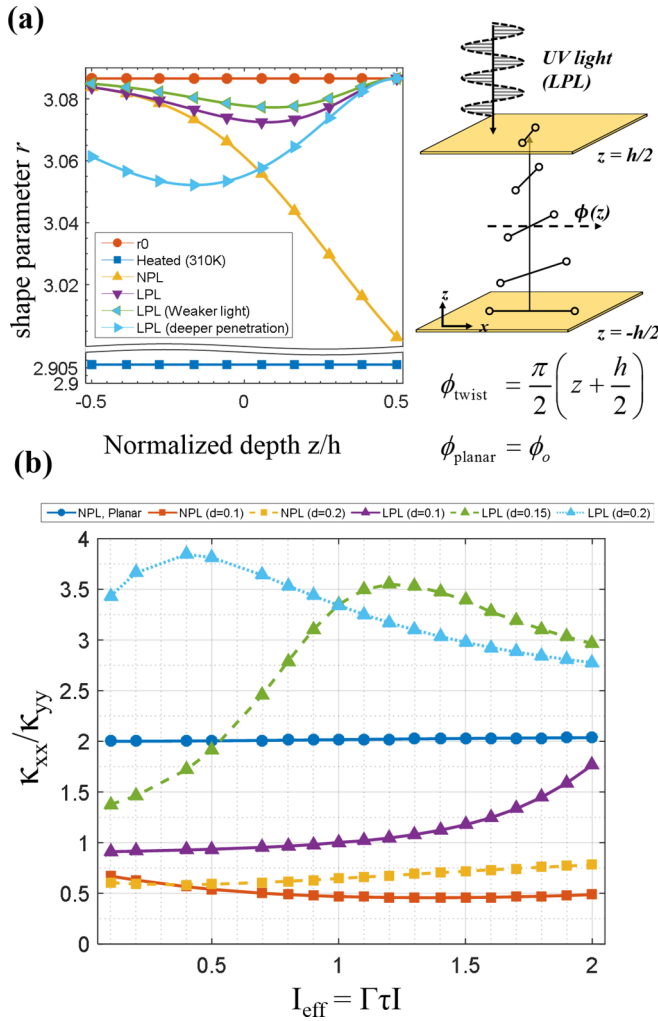


FIG. 8. (Color online) (a) Evolution of the shape parameter of the twisted configuration depending on external stimuli (NPL denotes nonpolarized light and LPL linearly polarized light in the x direction). (b) Ratio of principal curvatures with various external stimuli and penetration depths.

Increased intensity generates deeper and more isotropiclike behavior while retaining the general shape parameter profile. On the other hand, the penetration depth d strongly affects the behavior in terms of both value and depth of the shape parameter profile. Increased temperature simply shifts the profile, as the decaying influence is extracted from the model. Such a profile of shape parameter, by which the depth-varying principal direction of the eigenstress model is induced, emphasizes the modeling capability of the present work for two main reasons. First, additional aspects of shape parameters that change in the vertical direction can also be simulated, such as in the case of doped nanoparticles [37] and the positional modulations of azobenzene chromophores [36]. Second, a dependence of optical stimulus can be investigated with respect to the decaying profile and polarization.

Figure 8(b) shows the ratio of curvature of the LCN sheets. For all computations, the absorbance rate model was assumed to be equal to the planar mesogen alignment. The clamped condition was imposed only at the center of the squared sheet.

The lengths L_x and L_y were set to 10 mm and h was set equal to 0.5 mm. Distinctive trends are found depending on the irradiation condition. For LPL irradiation, where the order at the midsurface is mainly diluted due to the increased number of cis molecules, the ratio of curvatures converges around 2; roughly, such a value emerges when the bending momentum M_{xx} is about half of M_{yy} due to incompressibility and likewise for nonpolarized light with planar distribution $[\mathbf{n}_0 = (1, 0, 0)^T]$. The convergence profiles, however, vary extremely as penetration depth changes; as shown in Fig. 8(a), the photoisomerization mainly occurs at the midplane for light penetration depth, while uniaxial contractions were evoked near the bottom for deeper penetration. Similar remarks apply to nonpolarized light irradiation, wherein the photomechanical behaviors are governed only by light decay and the ratio converges around 0.5 for light penetration; uniaxial contraction dominates in this case. For higher penetration, on the other hand, the ratio converges to unity as light increases and mesogens isomerize uniformly, regardless of the thickness, which is analogous to the heated condition; although not reported herein, the heated condition produces exactly the same eigenstrain ($\kappa_{xx} = \kappa_{yy}$) as reported in Ref. [28]. It is worth mentioning that the thickness h is of critical importance in twisted configuration, in contrast to uniformly distributed mesogen, as the Kirchhoff assumption is often violated in the LCN structure due to transverse shear resulting from strain compatibility [28].

The disclination defect imprinted on the LCN directors is also studied. Radially distributed mesogens, for instance, induce contractile photostrain in the radial direction as well as positive photostrain in the azimuthal direction. Accordingly, geometric instability inevitably occurs and drives an initially 2D plate to become a 3D structure. Here we investigated a radial topology defect with a strength of +1, and with a missing row in the center, in order to demonstrate two aspects: the extent of external stimulation required for the instability onset and the reproduction of the experimentally reported topological changes.

In Fig. 9 we illustrate the disclination-driven instability produced by imprinted radially distributed mesogens and actuation due to the light irradiation and elevated temperature. A quarter of the model ($R_x = R_y = 20$ mm, with thickness 0.4) is simulated and clamped conditions are applied at the center node. The dramatic effect of nonlinearity is illustrated in Fig. 9(a). The two LCN sheets under different conditions are significantly different, even though they have similar geometric properties (i.e., thickness and radius) and are subject to the same stimulation conditions (i.e., temperature and light intensity). The difference stems from the geometric instability that arises from the radial distribution of light-induced strain and its Poisson effect. In the linear solution, the LCN behavior is bending dominated, yielding the sombrero shape. On the other hand, the LCN sheet becomes unstable following irradiation by light and exhibits bucklinglike behavior at the bifurcation point. The observed shape of anticlastic curvature with an apex at the center agrees well with recently reported experimental results [27,28,45]. Ground states from other mechanically frustrated cases, such as $s = -1$ and -2 , can also be solved via the same numerical method.

To quantify the bifurcation point, after which the nontrivial deformation solution can be obtained, a scaled standard

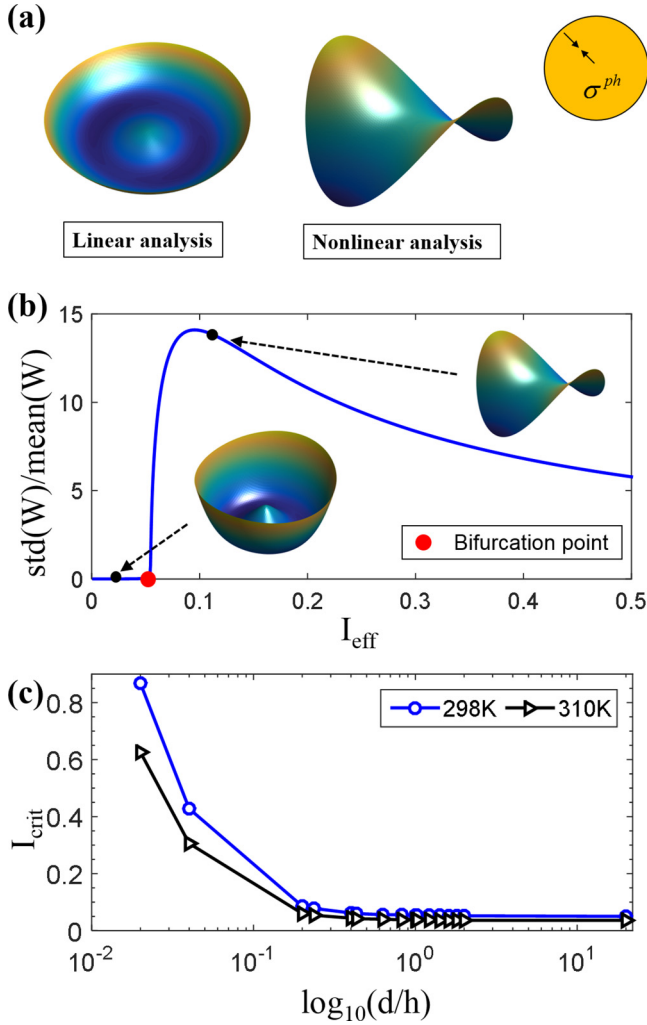


FIG. 9. (Color online) Shape change of the LCN sheet with radial disclination-defect-induced instability: (a) linear vs nonlinear solution, (b) instability onset, and (c) trends of critical intensity I_{crit} at the bifurcation point.

deviation of out-of-plane displacement shown at the boundary nodes W is proposed. The onset of instability is clearly illustrated in Fig. 9(b), where the threshold is set to 0.1. A sombrero shape is shown for the prebifurcation linear regime, whereas a saddle shape is observed elsewhere. The present study also discloses the dependence of the critical light intensity on temperature and d/h . According to this study, the critical intensity is smaller for increased depth of light penetration and continuously decreases even when d/h is much larger than unity. These phenomena are well explained by an analogy to an analytic solution of radial functionally graded material sheet instability [46], which suggests that only the ratio of the resultant membrane to bending rigidity N_{rr}^{ph}/D_{rr} contributes to the critical amount of external loading.

IV. CONCLUSION

Liquid-crystal networks are smart materials that accommodate large contraction and bending following optical and

thermal stimulation, suggesting their possible use in many attractive applications based on remote controllable actuation. In this paper we suggested a finite element framework designed for LCN films that incorporates a photomechanical constitutive model with a geometric nonlinear solution. For the multiphysical constitutive relation, the thermomechanical modeling suggested by Lin *et al.* [30] was employed along with an experimental phase behavior formula [11]; for geometric nonlinearity, an EICR [32] was used to attribute significant bending behavior that is often observed in experiment [9,10,13]. As the constitutive relation is composed of microstates of the polymeric conformation (i.e., shape parameter r and director \mathbf{n}), comprehensive analysis was facilitated via bridging large-scale macroscopic shape change with microscopic phase modulation. Several interrelated behaviors shown in LCNs were presented in order to demonstrate the enhanced simulation capability in both intrinsic and extrinsic conditions. The parametric studies with respect to the condition change explain how local small-scale behavior influences large-scale deformation.

We presented the light-induced bending curvature in terms of penetration depth and increasing light intensity. Nonlinearities that stem from the photobleaching effect were discussed, along with geometric rigid-body rotations. This finding suggests that the dependence of light-responsive LCN behavior on these parameters has to be established for better actuation system design, through either experiments or simulations of smaller scales.

Parametric studies regarding LCN film geometry were conducted. Motivated by experiment [13], flapping ellipsoidal LCN structures were simulated and discussed in terms of mechanical efficiency and the evolution of anticlasticity, both of which show nonlinearity and dependence on the aspect ratio. The global change of the mesogen director [7,8] was also investigated in terms of prospective actuation system design. We demonstrated that the alignment of the mesogen director alters the behavior from bending toward light to twisting and to bending away from light.

Finally, we investigated the effect of intrinsic, microscopic design parameters focusing on the spatially varying mesogenic alignment; the twist configuration, as one of the Fredericks distortions of nematic liquid crystals, was imposed within the element and stimulated through heating or polarized or nonpolarized light. The ratio of curvature, whose value is equal to unity under the heated condition [28], was found to vary depending on light intensity, polarization, and the penetration depth of the material. Furthermore, we also simulated the instability driven from $s = +1$ disclination texture to demonstrate that the current framework is able to reproduce ground-state result from mechanical frustration that are otherwise unattainable. In addition, we revealed the critical light intensities necessary to induce the buckling [13], while their trends are analogous to the analytic solution of compressive loading that destabilizes a circular plate.

On the basis of this study, it may be concluded that the comprehensive finite element model presented herein facilitates both the design and analysis of the LCN film by meeting the following criteria: (i) 3D full-sheet modeling with arbitrary boundary conditions and shape, (ii) geometric nonlinearity due to bending, where motion is

primarily attributable to rigid-body rotation of the element, and (iii) capturing the microstate evolution in the vertical direction. It is worth mentioning that the last criterion is especially pivotal for bridging large-scale deformation with microstate modulation and is suggested as a way to alter the LCN behavior.

The present research, however, is limited to sheets whose thicknesses are sufficiently small for applying in-plane stress and Kirchhoff-Love plate theory so as to retain the plane stress conditions. In the twisted mesogenic distortion, the thickness constraint should be taken more carefully as shear strain arises due to meeting the compatibility in the out-of-plane direction, although its strain energy decays by $O(h^2)$ and thus is neglected herein. For other Fredericks distortions (splay and bend) or homeotropic cases where out-of-plane

stress emerges, on the other hand, the stress conditions and resulting formulations need to be reformulated from scratch. Moreover, further quantitative studies are required as many material-related parameters are left hidden. For example, a molecular description of the penetration depth d has not been formulated so far. Therefore, either a sequential or concurrent multiscale description of the constitutive relation is highly demanded to turn phenomenological parameters into physical, quantitative parameters.

ACKNOWLEDGMENTS

This work was supported by the National Research Foundation of Korea funded by the Korean government (MSIP) (Grant No. 2012R1A3A2048841).

-
- [1] P.-G. de Gennes, *The Physics of Liquid Crystals* (Clarendon, Oxford, 1975).
- [2] A. Sánchez-Ferrer and H. Finkelmann, *Mol. Cryst. Liq. Cryst.* **508**, 348/[710] (2009).
- [3] D. Corbett and M. Warner, *Liq. Cryst.* **36**, 1263 (2009).
- [4] E. M. Terentjev and M. Warner, *Liquid Crystal Elastomers* (Clarendon, Oxford, 2006).
- [5] G. C. Verwey, M. Warner, and E. M. Terentjev, *J. Phys. II France* **6**, 1273 (1996).
- [6] S. M. Clarke, A. Hotta, A. R. Tajbakhsh, and E. M. Terentjev, *Phys. Rev. E* **64**, 061702 (2001).
- [7] Y. Yu, M. Nakano, and T. Ikeda, *Nature (London)* **425**, 145 (2003).
- [8] T. J. White, S. V. Serak, N. V. Tabiryan, R. A. Vaia, and T. J. Bunning, *J. Mater. Chem.* **19**, 1080 (2009).
- [9] K. D. Harris, R. Cuyper, P. Scheibe, C. L. van Oosten, C. W. M. Bastiaansen, J. Lub, and D. J. Broer, *J. Mater. Chem.* **15**, 5043 (2005).
- [10] A. Sánchez-Ferrer and H. Finkelmann, *Soft Matter* **9**, 4621 (2013).
- [11] P. M. Hogan, A. R. Tajbakhsh, and E. M. Terentjev, *Phys. Rev. E* **65**, 041720 (2002).
- [12] J. Choi, H. Chung, J.-H. Yun, and M. Cho, *Appl. Phys. Lett.* **105**, 221906 (2014).
- [13] M. Camacho-Lopez, H. Finkelmann, P. Palffy-Muhoray, and M. Shelley, *Nat. Mater.* **3**, 307 (2004).
- [14] M. Yamada, M. Kondo, J.-I. Mamiya, Y. Yu, M. Kinoshita, C. J. Barrett, and T. Ikeda, *Angew. Chem. Int. Ed. Engl.* **47**, 4986 (2008).
- [15] T. J. White, N. V. Tabiryan, S. V. Serak, U. A. Hrozhyk, V. P. Tondiglia, H. Koerner, R. A. Vaia, and T. J. Bunning, *Soft Matter* **4**, 1796 (2008).
- [16] J. J. Wie, D. H. Wang, K. M. Lee, L.-S. Tan, and T. J. White, *Macromolecules* **26**, 5223 (2014).
- [17] V. Toshchevikov, M. Saphiannikova, and G. Heinrich, *J. Phys. Chem. B* **113**, 5032 (2009).
- [18] J. M. Ilnytskyi, M. Saphiannikova, D. Neher, and M. P. Allen, *Soft Matter* **8**, 11123 (2012).
- [19] F. Cheng, R. Yin, Y. Zhang, C.-C. Yen, and Y. Yu, *Soft Matter* **6**, 3447 (2010).
- [20] M. Knežević and M. Warner, *Phys. Rev. Appl.* **2**, 044017 (2014).
- [21] M. Howard, J. Pajot, K. Maute, and M. L. Dunn, *J. Microelectromech. Syst.* **18**, 1137 (2009).
- [22] H. Wang, K. M. Lee, T. J. White, and W. S. Oates, *Macromol. Theor. Simul.* **21**, 285 (2012).
- [23] F. Cirak, Q. Long, K. Bhattacharya, and M. Warner, *Int. J. Solids Struct.* **51**, 144 (2014).
- [24] S. Conti, A. DeSimone, and G. Dolzmann, *J. Mech. Phys. Solids* **50**, 1431 (2002).
- [25] L. Jin, Z. Zeng, and Y. Huo, *J. Mech. Phys. Solids* **58**, 1907 (2010).
- [26] M. L. Dunn, *J. Appl. Phys.* **102**, 013506 (2007).
- [27] C. D. Modes and M. Warner, *Phys. Rev. E* **84**, 021711 (2011).
- [28] C. D. Modes, K. Bhattacharya, and M. Warner, *Proc. R. Soc. A* **467**, 1121 (2010).
- [29] W. Zhu, M. Shelley, and P. Palffy-Muhoray, *Phys. Rev. E* **83**, 051703 (2011).
- [30] Y. Lin, L. Jin, and Y. Huo, *Int. J. Solids Struct.* **49**, 2668 (2012).
- [31] L. Cheng, Y. Torres, K. M. Lee, A. J. McClung, J. Baur, T. J. White, and W. S. Oates, *J. Appl. Phys.* **112**, 013513 (2012).
- [32] C. A. Felippa and B. Haugen, *Comput. Methods Appl. Mech. Eng.* **194**, 2285 (2005).
- [33] H. Finkelmann, A. Greve, and M. Warner, *Eur. Phys. J. E* **5**, 281 (2001).
- [34] B. L. Mbanda, F. Ye, J. V. Selinger, and R. L. B. Selinger, *Phys. Rev. E* **82**, 051701 (2010).
- [35] D. Corbett and M. Warner, *Phys. Rev. Lett.* **99**, 174302 (2007).
- [36] A. Priimagi, A. Shimamura, M. Kondo, T. Hiraoka, S. Kubo, J.-I. Mamiya, M. Kinoshita, T. Ikeda, and A. Shishido, *ACS Macro Lett.* **1**, 96 (2012).
- [37] J. Xu, D. Bedrov, G. D. Smith, and M. A. Glaser, *Phys. Rev. E* **79**, 011704 (2009).
- [38] K. Katayama, Y. Choi, J. W. Kang, Z. Yaqoob, P. T. C. So, T. Fujii, S. Kuwahara, K. Takado, and T. Ikeda, *Phys. Chem. Chem. Phys.* **16**, 27074 (2014).
- [39] K. Y. Sze, X. H. Liu, and S. H. Lo, *Finite Elem. Anal. Des.* **40**, 1551 (2004).
- [40] C. A. Felippa, *Comput. Methods Appl. Mech. Eng.* **192**, 2125 (2003).

- [41] J.-L. Batoz, K.-J. Bathe, and L.-W. Ho, *Int. J. Numer. Methods Eng.* **15**, 1771 (1980).
- [42] A. M. Donald, A. H. Windle, and S. Hanna, *Liquid Crystalline Polymers* (Clarendon, Oxford, 2006).
- [43] L. Jin, Y. Yan, and Y. Huo, *Int. J. Non-Linear Mech.* **45**, 370 (2010).
- [44] H. T. Chen and L. H. He, *J. Phys.: Condens. Matter* **20**, 285107 (2008).
- [45] L. T. de Haan, C. Sánchez-Somolinos, C. M. W. Bastiaansen, A. P. H. J. Schenning, and D. J. Broer, *Angew. Chem. Int. Ed. Engl.* **51**, 12469 (2012).
- [46] M. M. Najafizadeh and M. R. Eslami, *Int. J. Mech. Sci.* **44**, 2479 (2002).